# Supporting Information

# Sustainable Non-Noble Metal Bifunctional Catalyst for Oxygen-Depolarized Cathode and $Cl_2$ Evolution in HCl Electrolysis

*Vikram Singh, Subhasis D. Adhikary, Aarti Tiwari, Debaprasad Mandal* and Tharamani C. Nagaiah**

Department of Chemistry, Indian Institute of Technology Ropar, Rupnagar, Punjab-140001, India

**Experimental:**

**General:** Glasswares used in the experiments were clearly washed and dried in oven before use. Composite and its precursors were vacuum dried at ~60 °C at $10^{-3}$ mbar pressure for 2h to ensure the maximum evaporation of free water molecules and volatile substances (if present in sample) before performing each test.

**Synthesis of OCNTs:** Synthesis of OCNT's was carried out in the gaseous phase as per the previously reported literature. [1] Briefly, CNT's were received from Applied Science Inc. (Ohio, USA) having inner diameters of 20-50 nm and outer diameters of 70-200 nm. To make sure that, as-received CNT's does not have aromatic impurities they were first treated at high temperature (800 °C) for one hour in He atmosphere. In order to obtain functionalized CNT's, the thermally treated CNT's were oxidized using $HNO_3$ in the vapor phase for 48 hours at 200 $^oC$, cooled for some time and then dried at 60$^oC$ overnight.

**Electrochemical Impedance Analysis:** Electrochemical impedance spectroscopy was performed to inspect the electrical properties of the catalysts in 3 mM $K_3[Fe(CN)_6]$ using 0.1 M KCl as supporting electrolyte. The measurements were performed by applying a DC potential of 0.2 V over and an AC perturbation of 10 mV for frequencies ranging from 0.1 Hz to 100 kHz in a logarithmic step. The Nyquist plot yields Rct (charge-transfer resistance) by subtracting the solution resistance (Rs, high frequency intercept of x-axis) from the polarization resistance (Rp, low frequency intercept of y-axis). The equivalent circuit applied to compute the various resistances was [R(Q[RW])] and the obtained $\chi^2$ value was 0.03. The feature observed at the low frequency region in both cases is due to the Warburg diffusion, corresponding to the diffusion of the reactant species to the macroscopic planar electrode surface.

**Physical characterization**

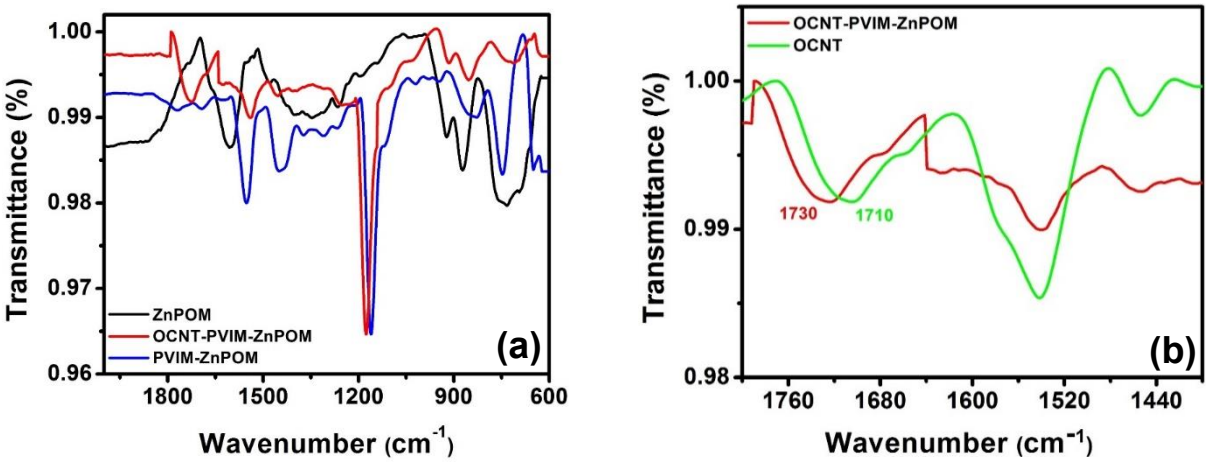


**Figure S1.** Comparative FT-IR spectra of (a) ZnPOM; PVIM-ZnPOM and OCNT-PVIM-ZnPOM; (b) OCNTs and OCNT-PVIM-ZnPOM for interaction studies.

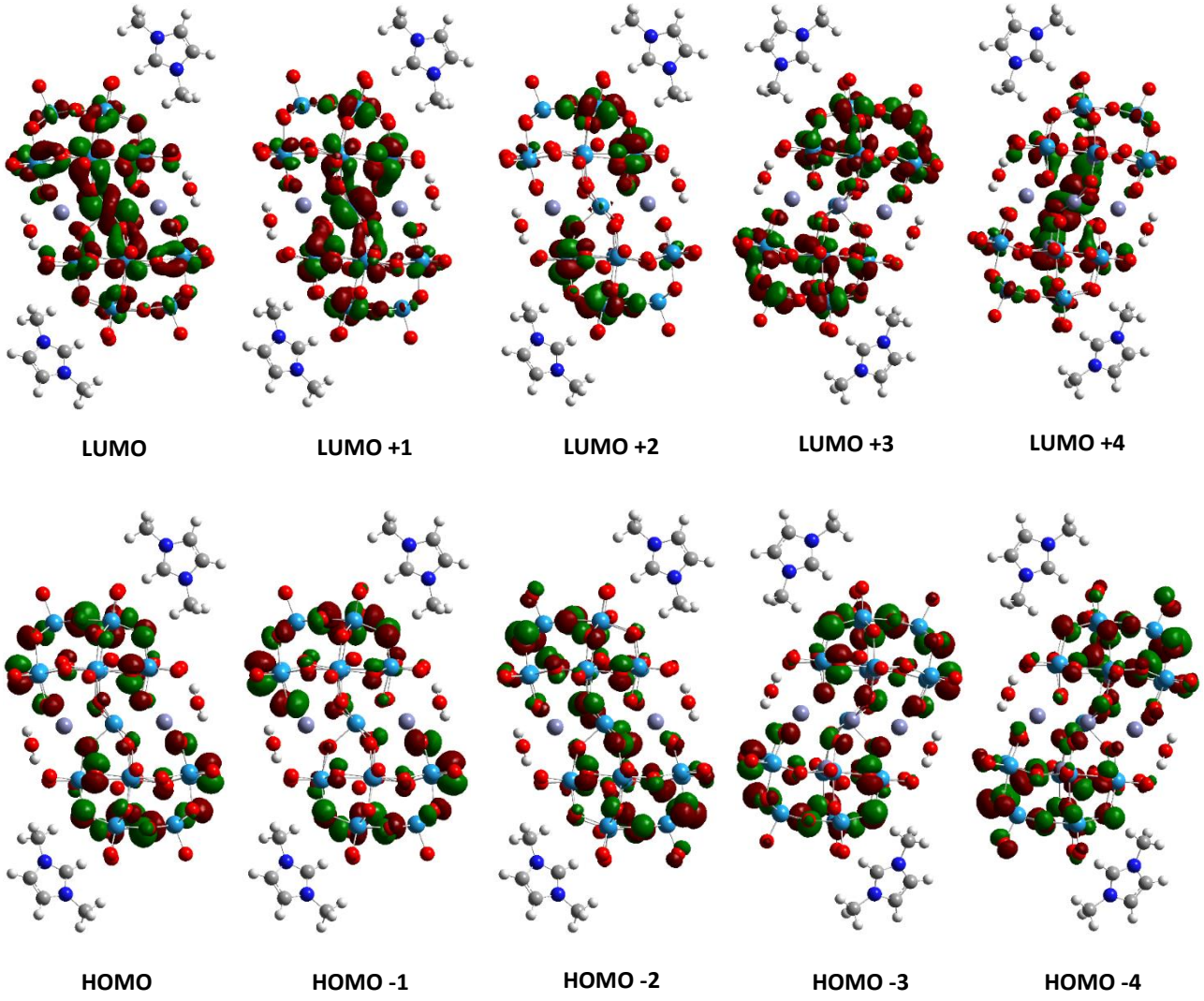


**Figure S2.** HOMO-LUMO molecular orbitals of $[Me2Imd]_2\ [WZn_3(H_2O)_2(ZnW_9O_{34})_2]^{10-}$.

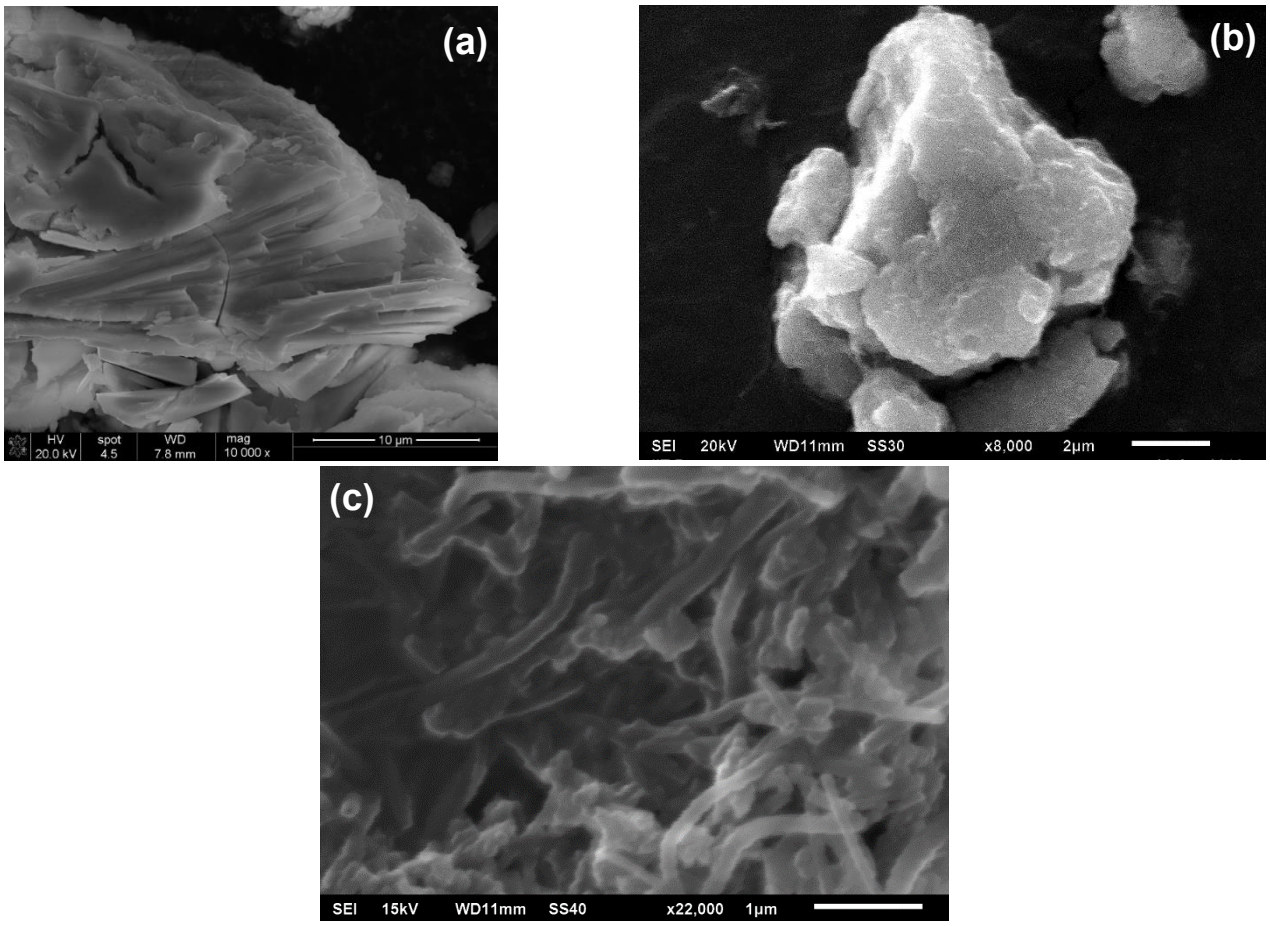


**Figure S3.** SEM images for (a) ZnPOM; (b) PVIM-ZnPOM and (c) OCNT-PVIM-ZnPOM composite.

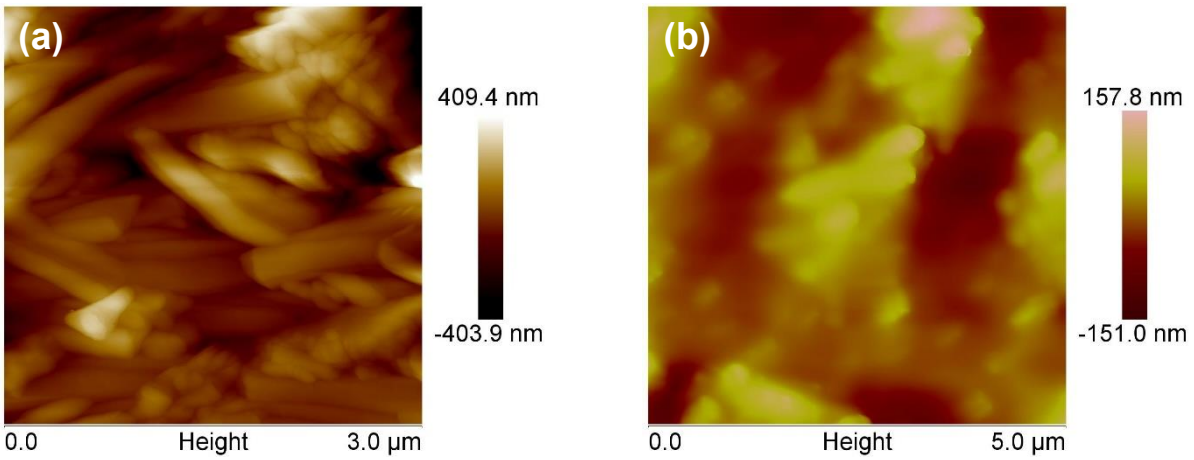


**Figure S4.** AFM images of (a) OCNT and (b) OCNT-PVIM.

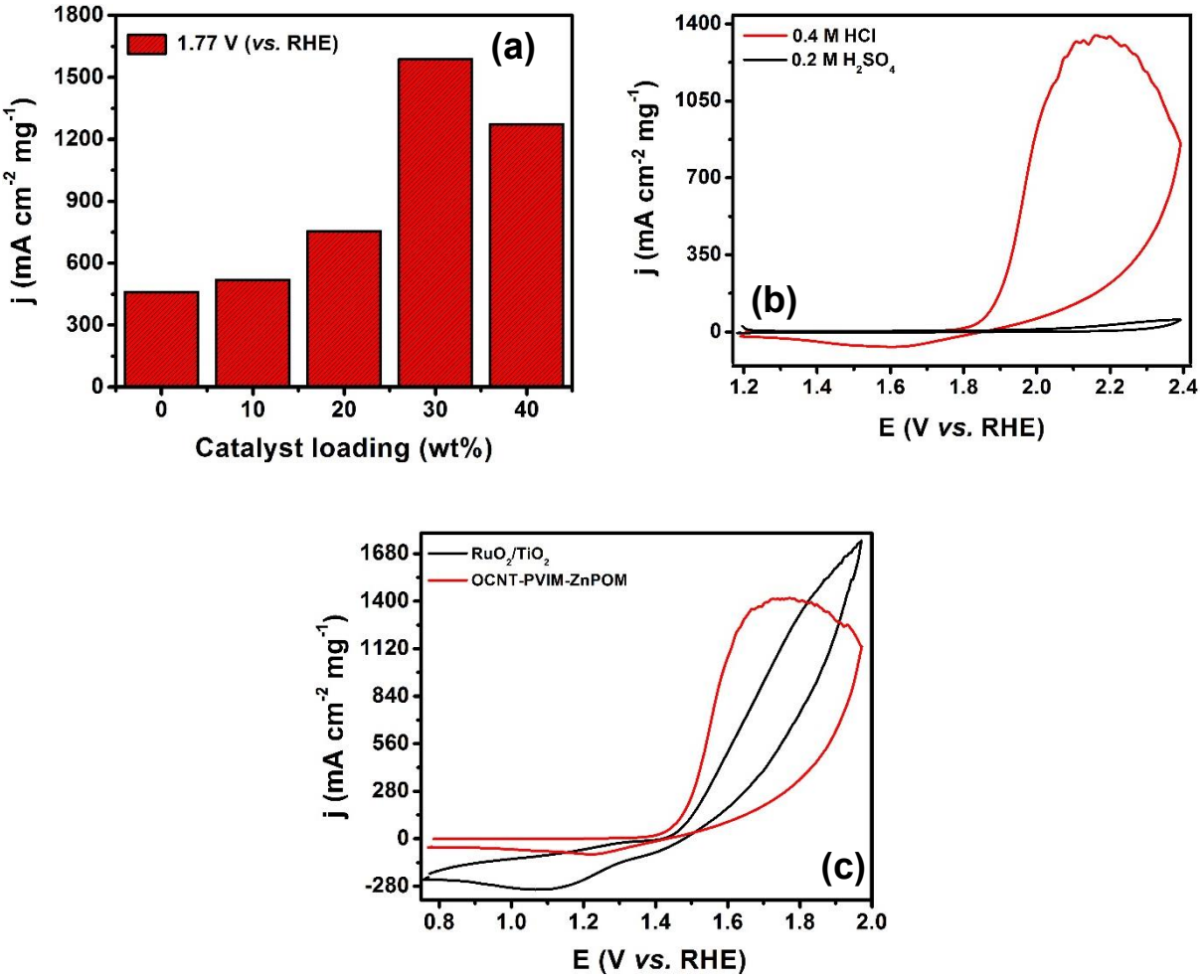


**Figure S5.** (a) Bar diagram representing optimization of the catalyst conjugate (PVIM-ZnPOM) loading over the conductive OCNT support; (b) Cyclic voltammogram for OCNT-PVIM-ZnPOM in $N_2$ saturated 0.4 M HCl and 0.2 M $H_2SO_4$ electrolyte and (c) Cyclic voltammogram for OCNT-PVIM-ZnPOM and $RuO_2/TiO_2$ (synthesized hydrothermally following *Scientific Reports* **2012**, 2, 801) in 0.4 M HCl at a scan rate of 10 mV $s^{-1}$. CE: Pt mesh; RE: Ag/AgCl/3M KCl.

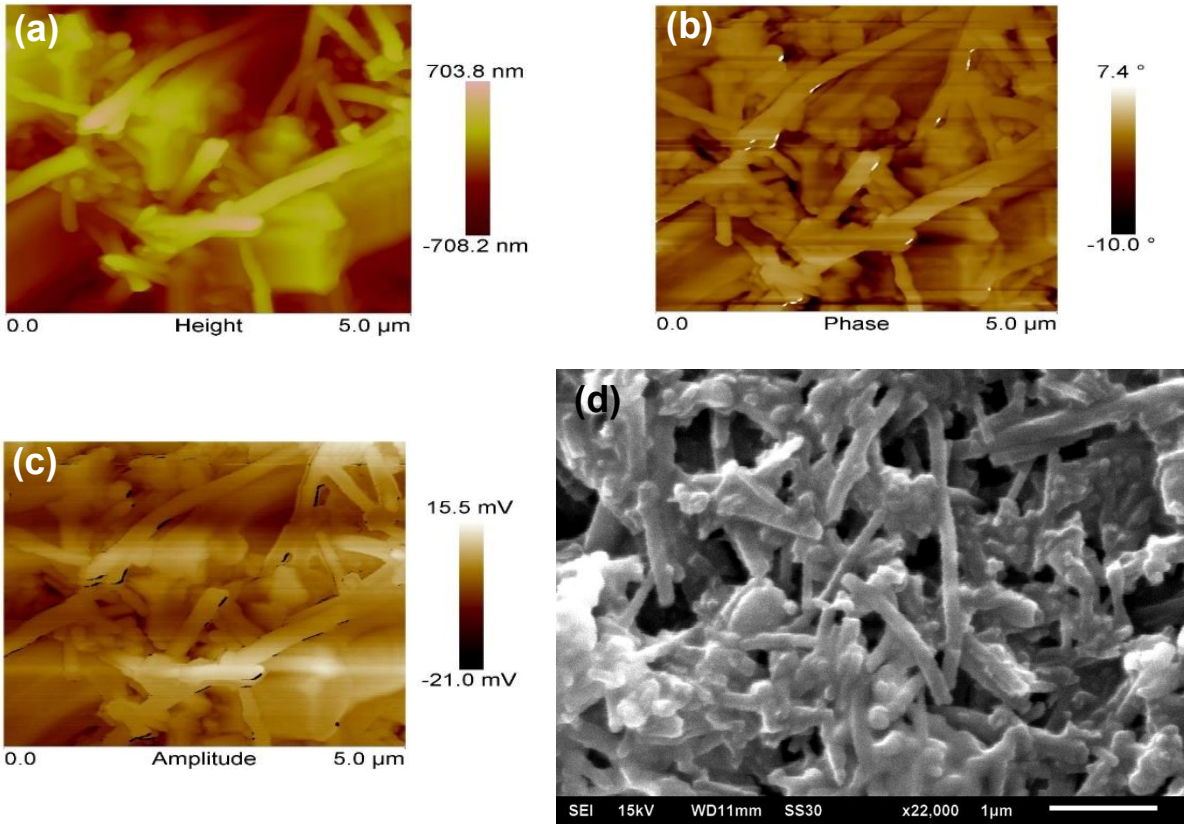


**Figure S6.** (a) AFM images (b) phase (c) electrostatic force microscopic image and (d) corresponding SEM image of OCNT-PVIM-ZnPOM after prolonged electrolysis.

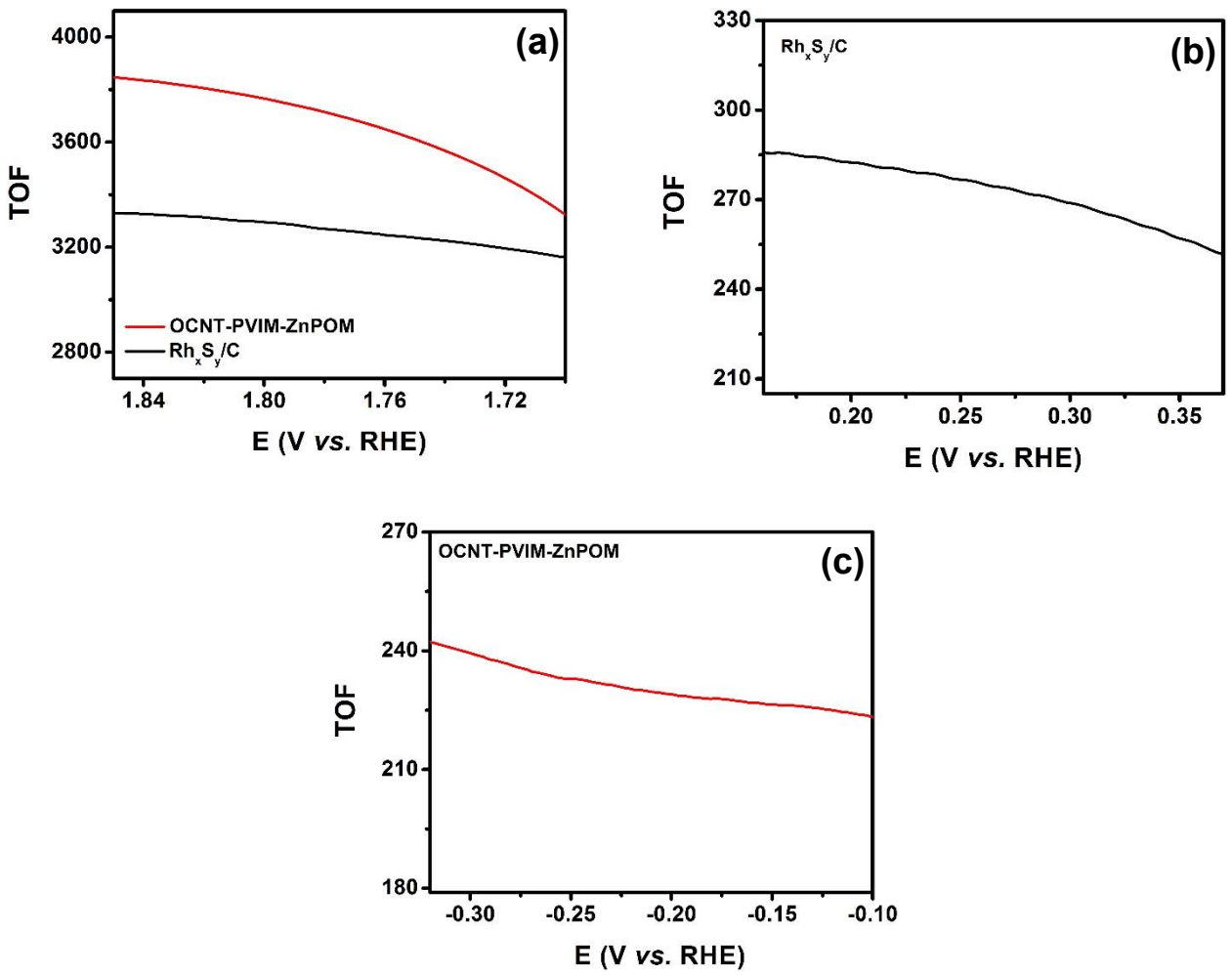


**Figure S7.** (a) Mass specific turnover frequency (TOF) per *mg* of OCNT-PVIM-ZnPOM composite and $Rh_xS_y/C$ for chlorine evolution; (b) turnover frequency per *mg* of $Rh_xS_y/C$ and (c) OCNT-PVIM-ZnPOM for oxygen reduction reaction. CE: Pt mesh; RE: Ag/AgCl/3 M KCl.

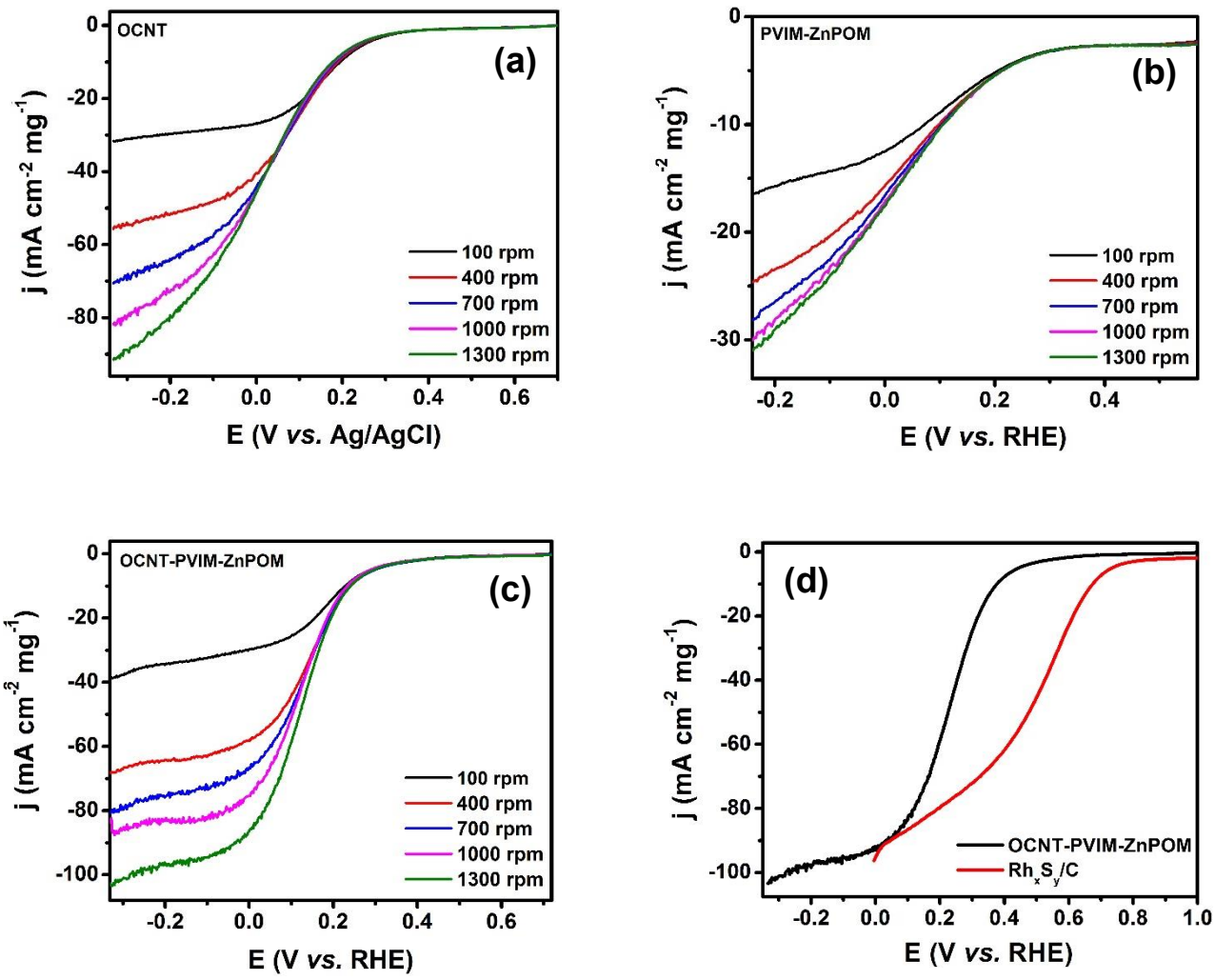


**Figure S8.** Hydrodynamic linear sweep voltammograms of (a) OCNT, (b) PVIM-ZnPOM, (c) OCNT-PVIM-ZnPOM at different rotation rates and (d) comparison between OCNT-PVIM-ZnPOM and $Rh_xS_y/C$ at 1300 rpm in $O_2$ saturated 0.4 M HCl electrolyte with a scan rate of 5 mV $s^{-1}$. CE: Pt mesh; RE: Ag/AgCl/3M KCl.

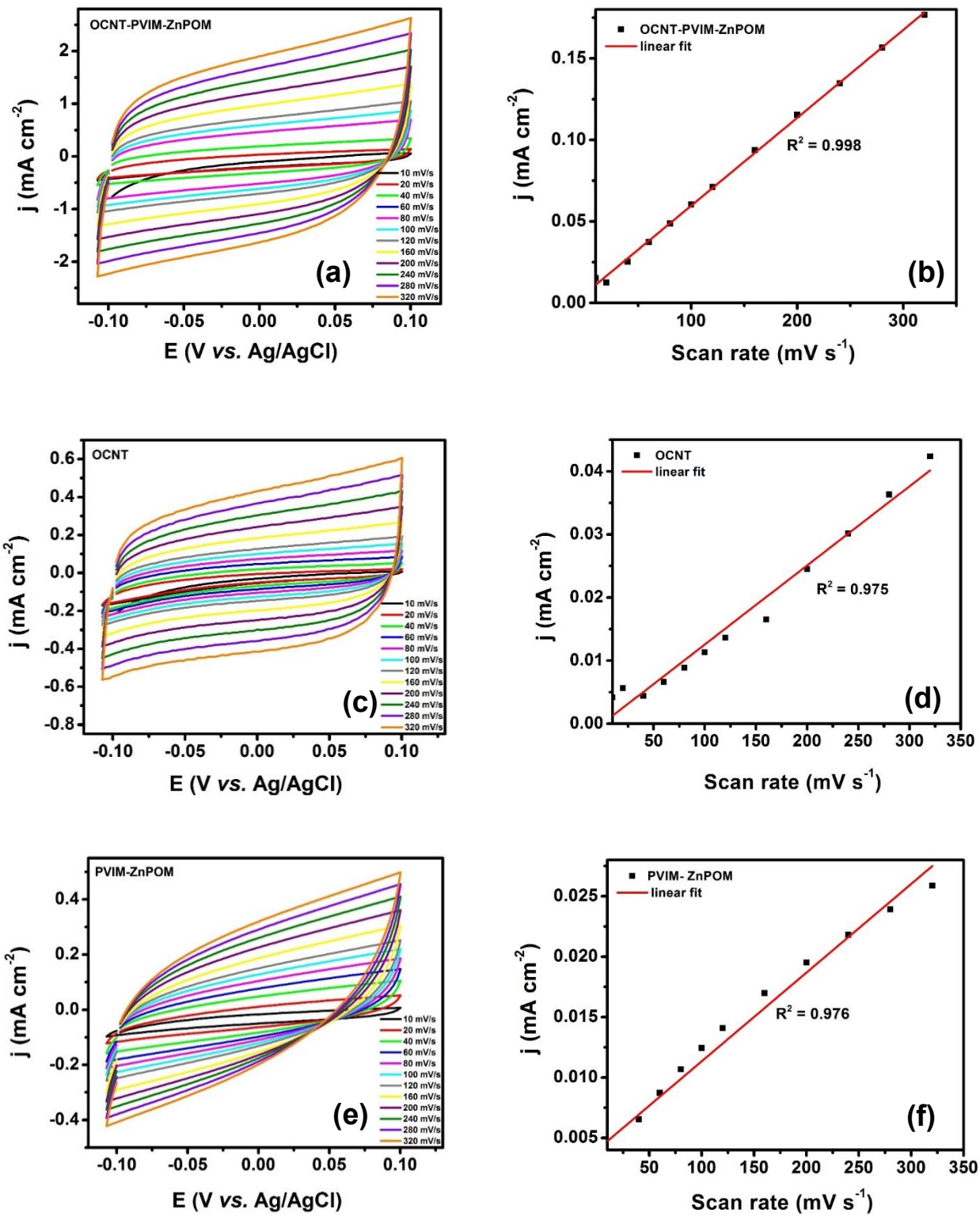


**Figure S9.** (a); (c) & (e) Cyclic voltammograms and their corresponding, (b); (d) & (f) average current density versus scan rate for OCNT-PVIM-ZnPOM composite, OCNT and PVIM-ZnPOM conjugate respectively over non-faradic potential range at variable scan rates in 0.4 M HCl electrolyte. CE: Pt mesh; RE: Ag/AgCl/3 M KCl.

**Electrochemical surface area (ECSA) Analysis:**

The fact that OCNT-PVIM-ZnPOM composite is electrochemically more accessible towards ORR catalytic process is hinted by the electrochemical surface area (ECSA) determination. It is well known that larger the ECSA higher will be the electrocatalytic activity towards ORR. In this study, ECSA was calculated using electrochemical capacitance measurements by sweeping potentials in the non-faradic regime from -100 mV to 100 mV (*vs.* Ag/AgCl) at different scan rates (10, 20, 40, 60, 80, 100, 120, 160, 200, 240, 280 and 320 mV $s^{-1}$) for each catalyst (Figure S9, SI). The double-layer capacitance was determined at a particular potential (0.0 V *vs.* Ag/AgCl) in the non-faradic potential region by plotting current density as a function of scan rate, from this linear fit we obtain the double-layer capacitance which was found to be 539.2 (μF $cm^{-2}$) for OCNT-PVIM-ZnPOM composite. The electrochemical surface area was determined by dividing the obtained double-layer capacitance by the capacitance for bare GCE (flat surface). [2] The surface area of various catalyst with different ESCA value was found to be 280.8 $cm^{-2}$ $mg^{-1}$, higher than the 65.1 $cm^{-2}$ $mg^{-1}$, 38.2 $cm^{-2}$ $mg^{-1}$ and 140.6 $cm^{-2}$ $mg^{-1}$ for OCNT-PVIM-ZnPOM, OCNT, PVIM-ZnPOM and $Rh_xS_y$/C (30%) catalysts respectively (**Table S3**, **SI**). The difference observed in ECSA is supposed to be due to strong interaction between OCNTs and PVIM-ZnPOM, and the porous nature of OCNTs facilitates the electron between electrode-electrolyte interface which is supported from EIS, IR, and EFM studies. These capacitive measurements there by hint that OCNT-PVIM-ZnPOM have higher electroactive surface area and hence exhibits increased electrocatalytic activity towards HCl electrolysis which includes both $Cl_2$ evolution and $O_2$ reduction. Further as it is clear from DFT studies, the HOMO orbitals are mostly contributed from oxygen atoms and no metal center is involved (**Figure 2**).

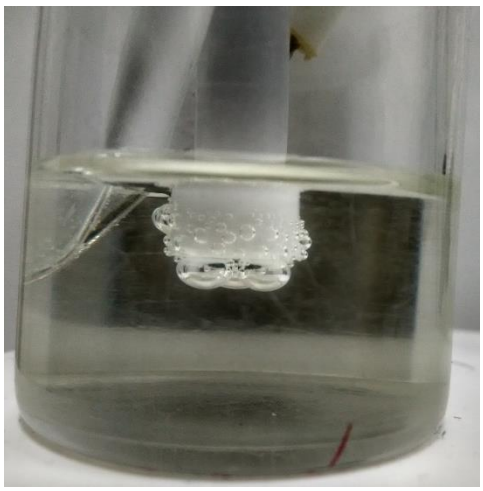

**Figure S10.** Photographic image of profusely evolved chlorine after continuous 3 days of HCl oxidation under 1000 rpm.

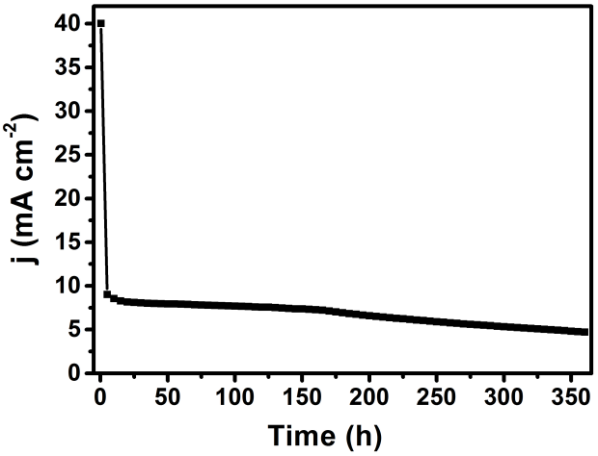


**Figure S11.** Chronoamperometric analysis of OCNT-PVIM-ZnPOM in 0.4 M HCl electrolyte at 1.77 V for 360 h. CE: Pt mesh; RE: Ag/AgCl/3M KCl.

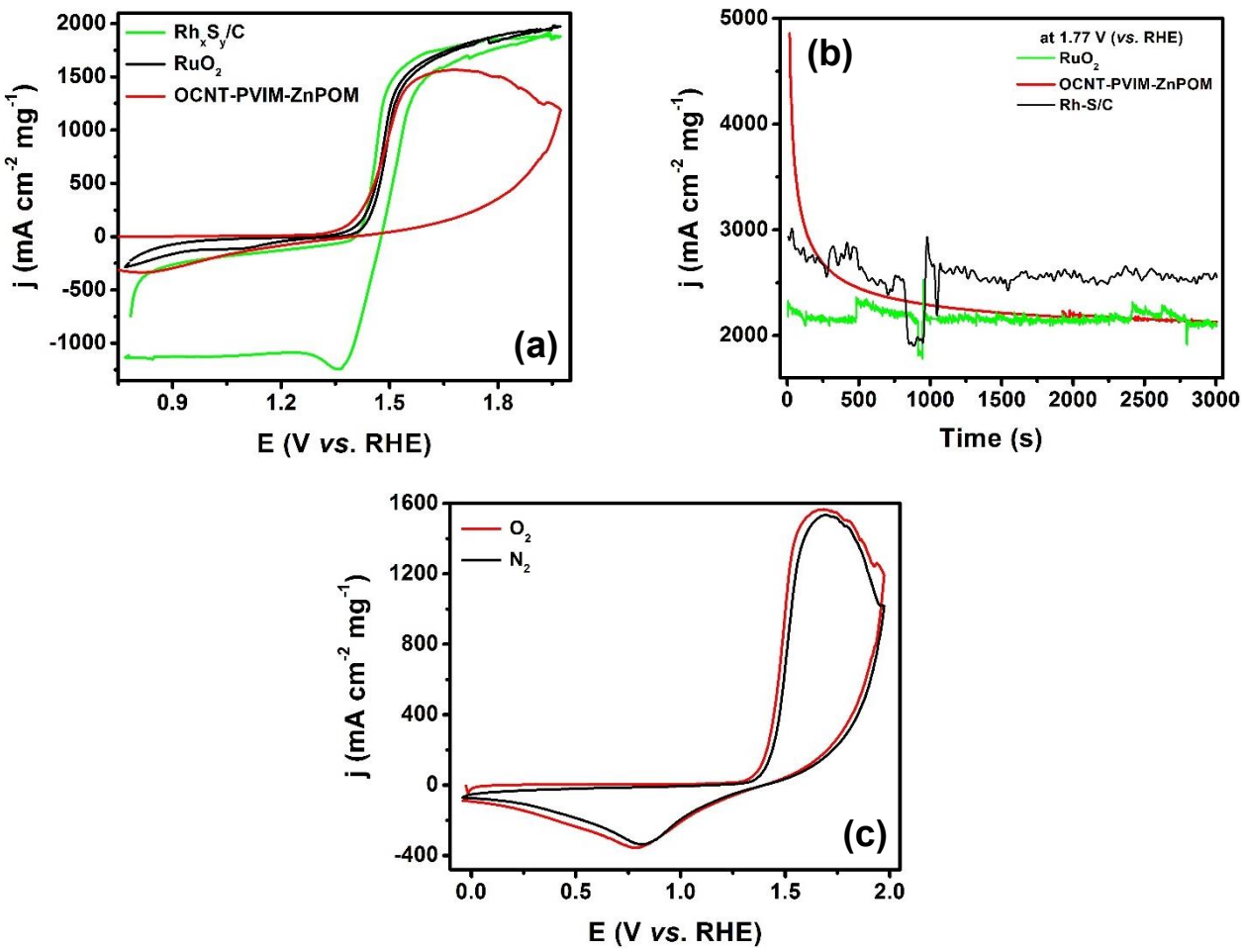


**Figure S12.** (a) Cyclic voltammogram at a scan rate of 10 mV $s^{-1}$ and (b) Chronoamperometric analysis at 1.77 V for OCNT-PVIM-ZnPOM *vs.* $Rh_xS_y$/C (30%) and $RuO_2$ in 5.0 M HCl electrolyte; (c) Cyclic voltammograms of OCNT-PVIM-ZnPOM in 5.0 M HCl electrolyte in presence and absence of oxygen. CE: Pt mesh; RE: Ag/AgCl/3M KCl.

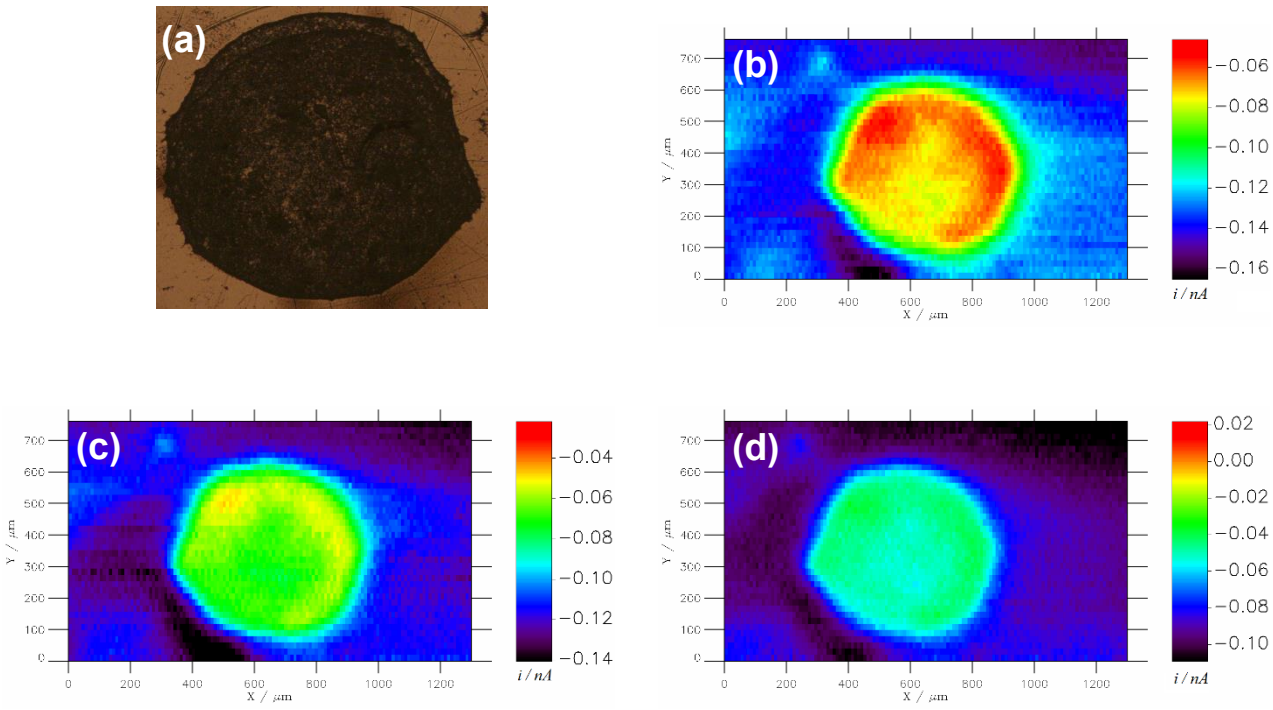


**Figure S13.** (a) Microscopic photograph of OCNT-PVIM-ZnPOM over GC plate after performing RC-SECM analysis for 48 h towards oxygen reduction reaction (ORR); 2-D representation of RC-SECM image (Fig. 10 of main text) at sample polarization potentials of (b) -0.13 V; (c) 0.07 V; and (d) 0.42 V respectively with the Pt-tip (10 µm Ø) held at 0.12 V.

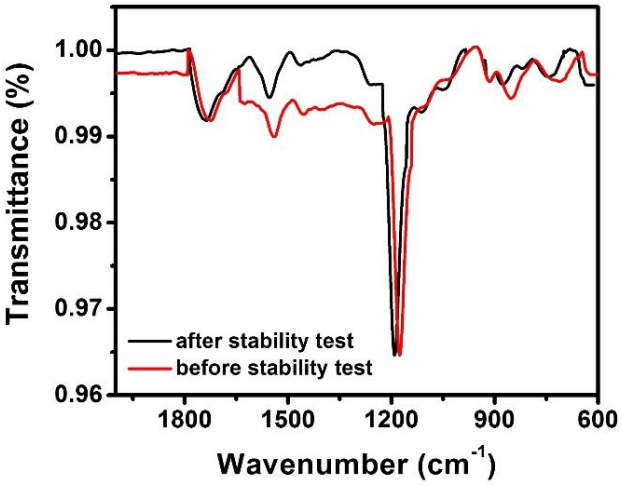


**Figure S14.** IR spectra of OCNT-PVIM-ZnPOM before and after prolonged LSV of 500 cycles for oxygen reduction condition in presence of $Cl_2$ gas in 0.4 M HCl electrolyte.

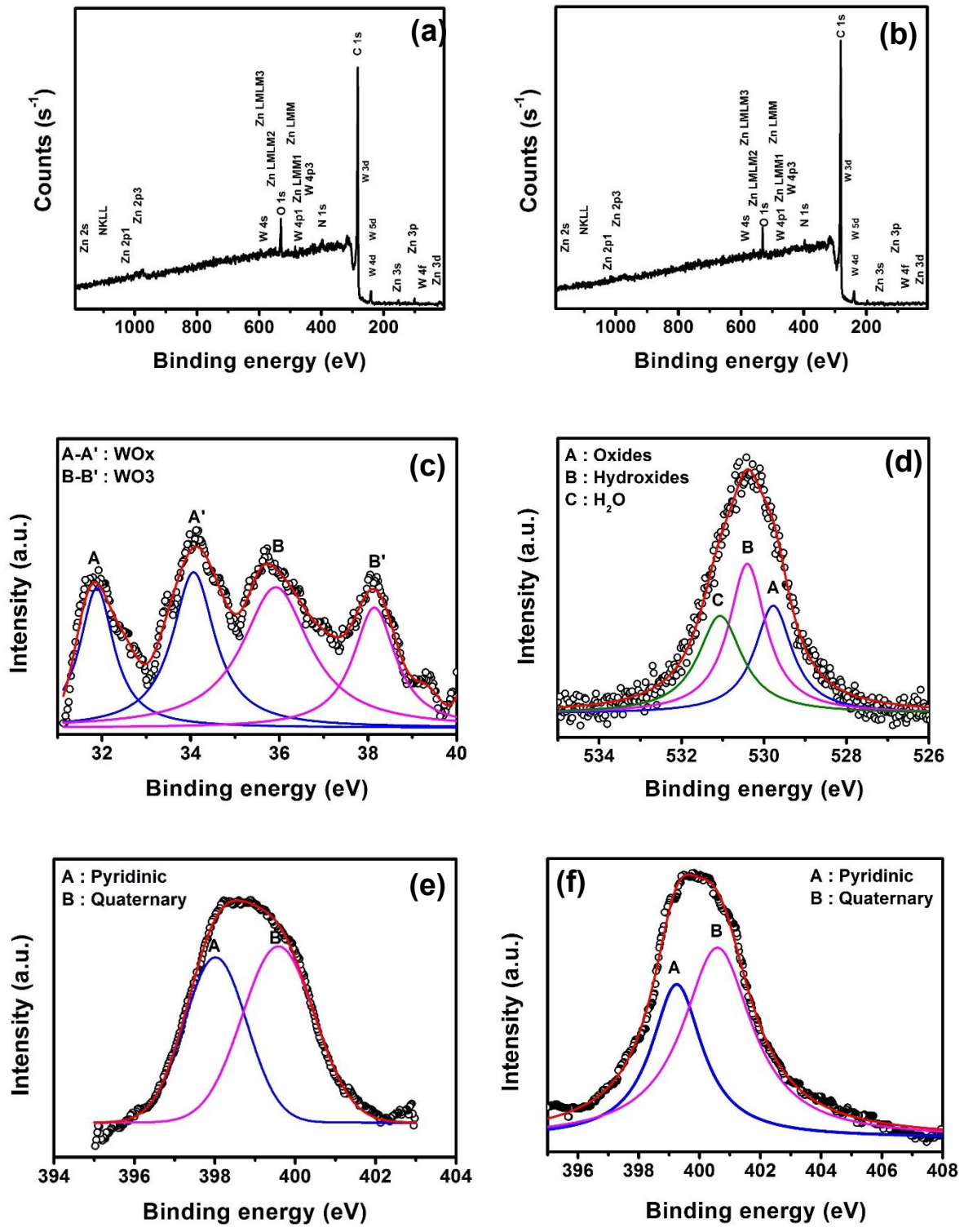


**Figure S15.** XPS survey spectra for OCNT-PVIM-ZnPOM composite (a) before and (b) after prolonged electrolysis; with individual deconvoluted XP spectra of (c) W4f; (d) O1s; after electrolysis (48 h) (e) & (f) N1s before and after electrolysis (48 h) respectively.

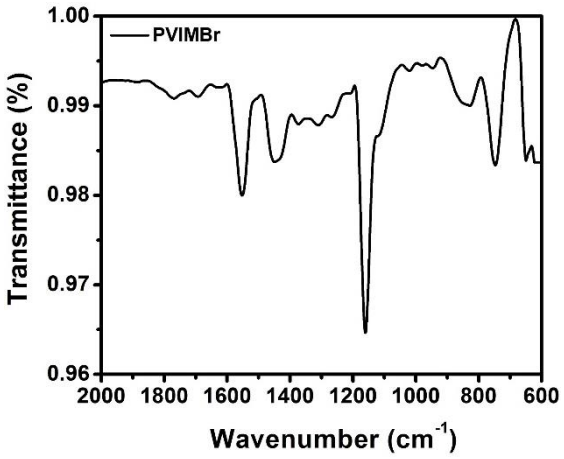


**Figure S16.** FT-IR spectra of poly-vinyl butyl imidazolium bromide (PVIM-Br).

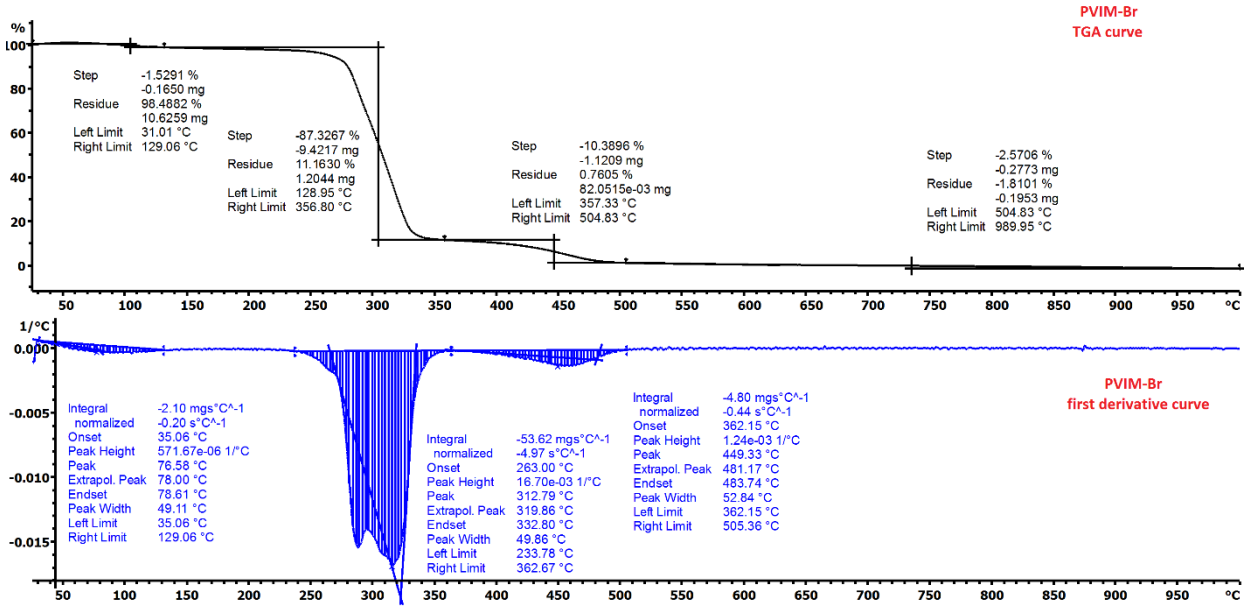


**Figure S17.** TGA and first derivative TGA curve of poly-vinyl butyl imidazolium bromide (PVIM-Br).

Thermal stability of ZnPOM, PVIM-Br and the composite PVIM-ZnPOM were checked by thermogravimetric analysis (TGA). The analysis was performed at a heating rate of 10 °C $min^{-1}$, from 25 °C to 1000 °C. The thermal decomposition temperature (Td) is considered as the onset temperature in TGA curves. The obtained curves represent that ZnPOM shows good thermal stability which is also reflected in the composite PVIM-ZnPOM. The water molecules from hydration sphere of ZnPOM evaporated in the temperature range of 50−125 °C. Integration of the obtained TGA curves resulted in 15 $H_2O$ molecules around ZnPOM molecule.

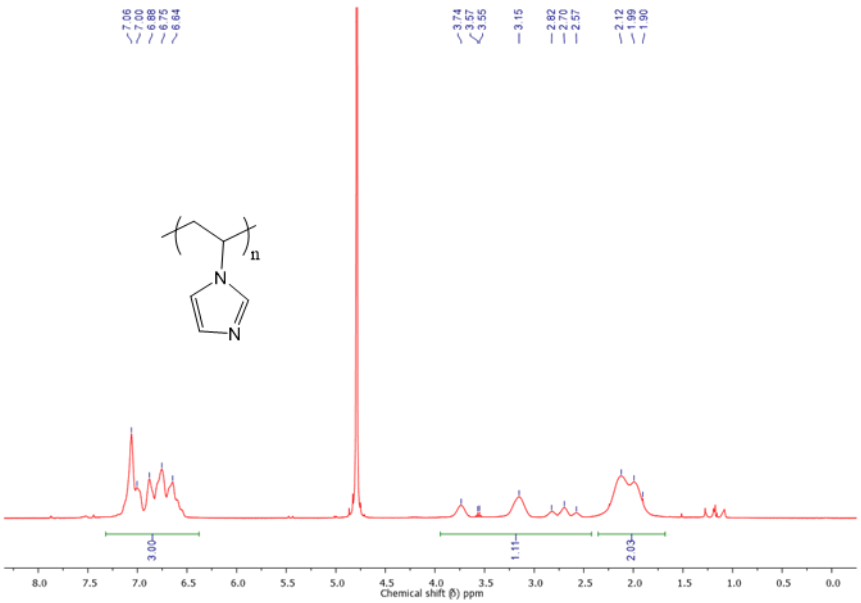


**Figure S18.** $^{1}$H NMR spectrum of Poly(1-vinylimidazole).

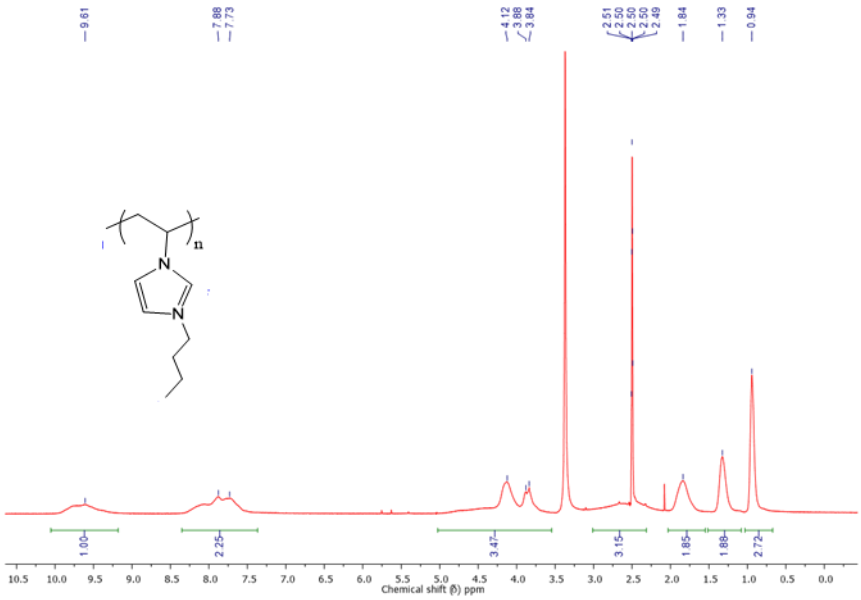


**Figure S19.** $^{1}$H NMR spectrum of Poly(1-vinyl butyl imidazolium bromide) (PVIMBr).

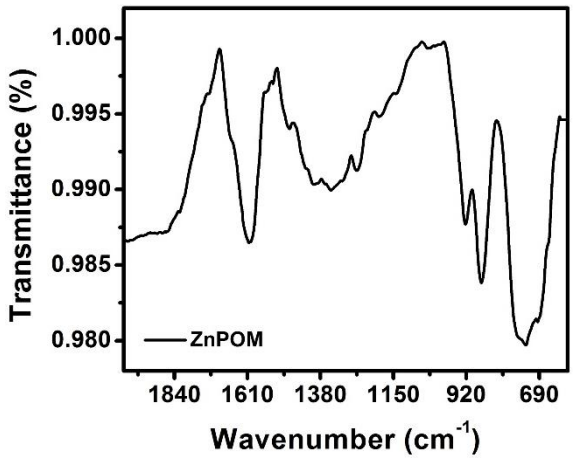


**Figure S20.** FT-IR spectra of ZnPOM.

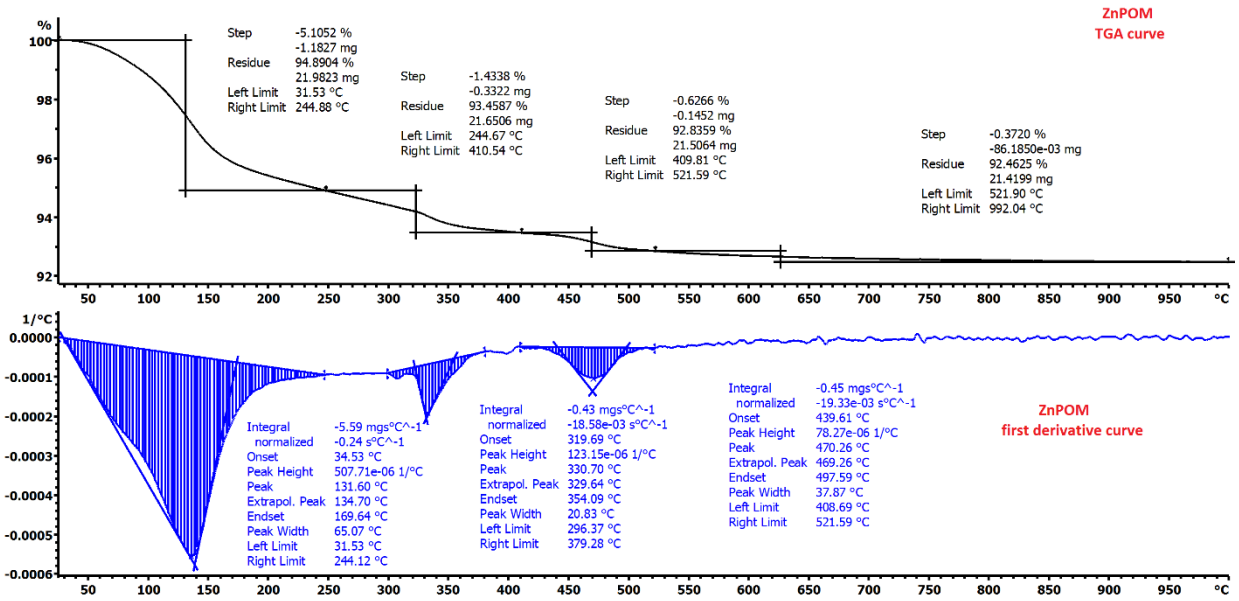


**Figure S21.** TGA and first derivative TGA curve of ZnPOM.

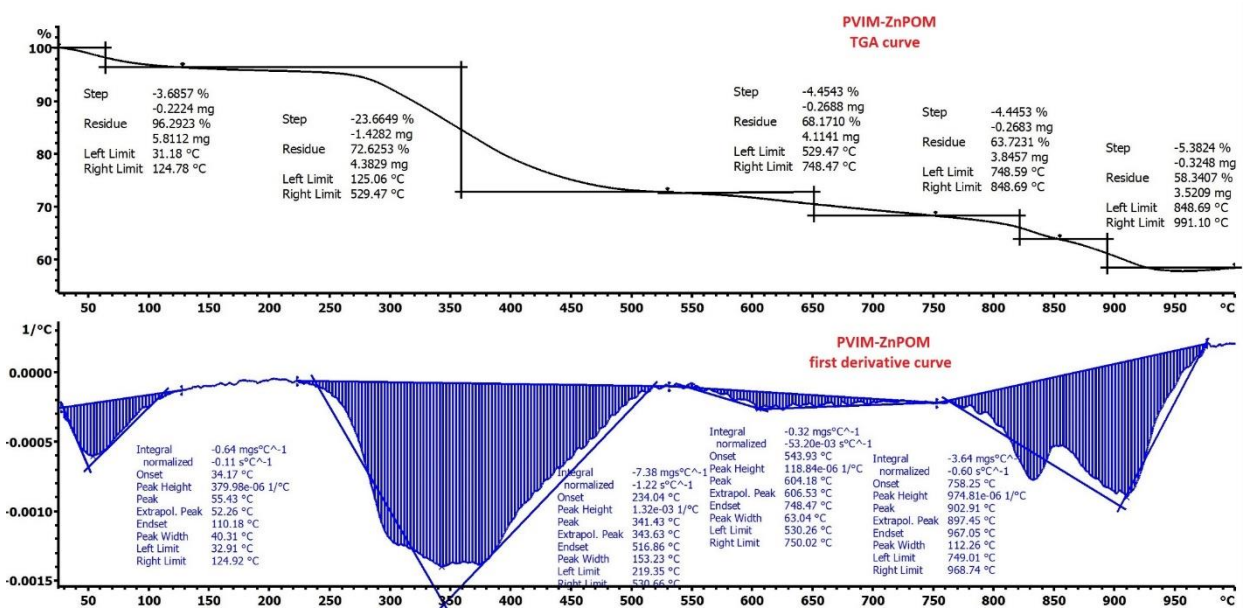


**Figure S22.** TGA and first derivative TGA curve of PVIM-ZnPOM.

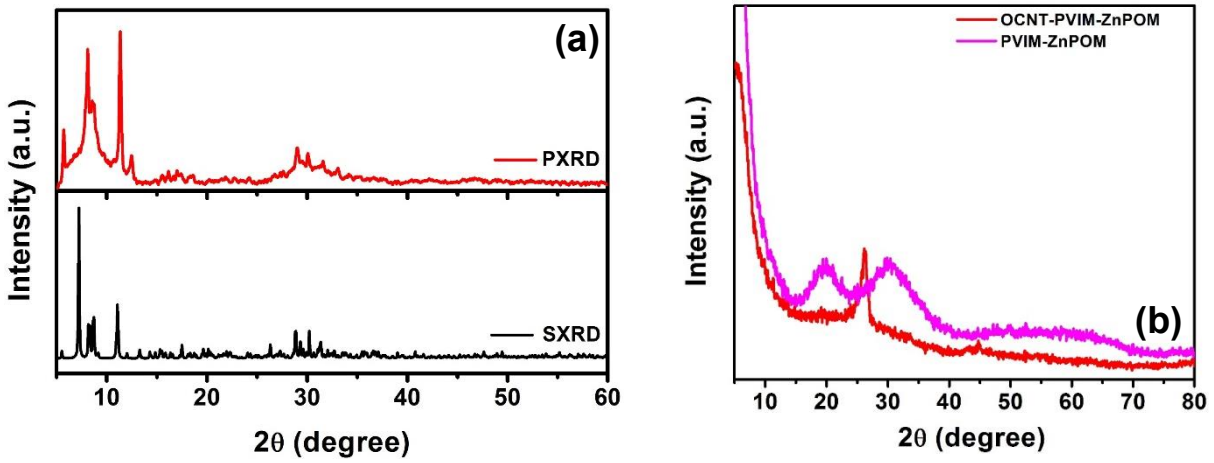


**Figure S23.** (a) PXRD and SXRD pattern for ZnPOM; (b) comparative PXRD of OCNT-PVIM-ZnPOM and PVIM-ZnPOM.

Powder X-ray diffraction (PXRD) study provided valuable information about the structural properties of the composite OCNT-PVIM-ZnPOM. The above figure shows XRD patterns for PVIM-ZnPOM and OCNT-PVIM-ZnPOM. The peaks corresponding to OCNT are very sharp and highly intense indicating the crystalline nature of carbon nanotube.[3] The diffraction peak for OCNT at $2\Theta = 26.03°$ corresponds to the (002) plane and the one around 43° for (001) plane of graphite. The XRD peaks around $2\Theta = 19.8°$ and 31.2° for PVIM-ZnPOM are broadened and less intense indicating the amorphous or polymeric nature of the PVIM, whereas ZnPOM does not show any characteristic peak in the powder XRD. In case of OCNT-PVIM-ZnPOM both the peaks for PVIM-ZnPOM tends to disappear which indicates strong interaction between the OCNT and PVIM-ZnPOM and this is also supported by FT-IR.

**Determination of $Cl_2$ evolution by Iodometric titration:**

The amount of chlorine evolved after 500 cycles of LSV by the catalyst was determined by iodometric titration with 0.1 mM $Na_2S_2O_3$. It was found that 5.82 mg/L or 5.82 ppm $Cl_2$ was evolved.

**Calculation:**

$Cl_2 + KI \rightarrow I_3^- + Cl^-$ (1)

$I_3^- + 2\ S_2O_3^{2-} \rightarrow 3I^- + S_4O_6^{2-}$ (2)

Total volume of 0.1 mM $Na_2S_2O_3$ consumed during titration = 41 mL

Volume taken in the flask (0.4 M HCl and 1 mM KI) = 25 mL

On applying the molarity equation

$M_1V_1 = M_2V_2$

0.1 mM x 41 mL = $M_2$ X 25 mL; $M_2 = 0.164$ mM ($I_3^-$)

From the stoichiometric equation 2 thio molecules are required for 1 $I_3^-$, so concentration of thio is equal to 0.082 mmol.

Amount of chlorine present in the solution = $0.082 * 10^{-3}$ mol/l * 71 g/mol = 5.82 mg/l or 5.82 ppm

| **Table S1: Iodometric titration for chlorine determination.** | | |
|---|---|---|
| **Sample** | **Mean Volume of $Na_2S_2O_3$ (ml)** | **$Cl_2$ evolved[*] (ppm)** |
| OCNT-PVIM-ZnPOM | 41.0 | 5.82 |
| $Rh_xS_y$/C | 42.2 | 5.99 |
| [*]Catalyst amount was 48 µg. | | |

**Turn over frequency calculation:[4]**

$$\text{TOF} = \frac{\#\ \text{total water}/Cl_2\ \text{turnover}\ /\ cm^2\ \text{geometrical area}}{\#\text{surface sites}\ /\ cm^2\text{geometrical area}}$$

Total number of water / $Cl_2$ turn overs can be calculated using current density as follows;

$$\#\ H_2O/Cl_2 = j\ \left(\frac{mA}{cm^2}\right)\left(\frac{1\ Cs^{-1}}{1000\ \text{mA}}\right)\frac{(1\ \text{mol of}\ e^-)}{96500\ \text{C}}\ \left(\frac{1\ \text{mol of}\ H_2O/Cl_2}{2\ \text{mol of}\ e^-}\right)\left(\frac{6.022\times10^{23}}{1\ \text{mol of}\ H_2O/\ Cl_2}\right)$$

$$= \mathbf{3.12 * 10^{15}}\ \frac{H_2O/Cl_2\ \text{per sec}}{\text{cm}^2}\quad \text{per mA/cm}^2$$

Surface sites per real surface area can be calculated as follows;

$$\#\ \text{Surface sites} = \frac{\text{No. of atoms / unit cell}}{(\text{Volume of the unit cell Å}^3)^{2/3}}$$

$$\text{TOF} = \frac{3.12 * 10^{15}\ H_2O/Cl_2\ s^{-1}cm^{-2}}{\#\ \text{surface active site} * \text{mass}}\ \text{per mA/cm}^2\ *\ (j)$$

| **Table S2: Surface site determination.** | | | |
|---|---|---|---|
| **Sample** | **No. of atoms/ unit cell** | **Unit cell volume ($Å^3$)** | **Surface sites* (atoms $cm^{-2}_{real}$)** |
| OCNT-PVIM-ZnPOM | 24 | 2437.23 | $1.326*10^{15}$ |
| $Rh_xS_y/C$[5] | 6 | 6494 | $0.172*10^{15}$ |
| *w.r.t electrochemical surface area | | | |

| **Table S3: Electrochemical surface area (ECSA) determination.** | | | | |
|---|---|---|---|---|
| **S. No.** | **Sample** | **$C_{dl}$* (µF) at 0.00 V** | **ECSA ($cm^{-2}$)** | **Roughness factor (a.u.)** |
| 1 | OCNT-PVIM-ZnPOM | 539.2 | 13.48 | 190.6 |
| 2 | OCNT | 125 | 3.125 | 44.2 |
| 3 | PVIM-ZnPOM | 73.41 | 1.835 | 25.9 |
| 4 | $Rh_xS_y/C$ | 270 | 6.75 | 95.47 |
| * Double layer capacitance | | | | |

| **Table S4: XPS analysis.** | | | | | |
|---|---|---|---|---|---|
| **Sample** | **C** | **O** | **Zn** | **W** | **N** |
| OCNT | 82.5 | 17.5 | - | - | - |
| OCNT-PVIM-ZnPOM (before)* | 92.4 | 5.7 | 0.2 | <0.1 | 1.7 |
| OCNT-PVIM-ZnPOM (after)* | 92.8 | 5.4 | 0.2 | 0.1 | 1.6 |
| *Analysis prior and post to prolonged electrolysis (48 h). | | | | | |

| **Table S5: EDAX analysis.** | | | | | |
|---|---|---|---|---|---|
| **Sample** | **C** | **O** | **Zn** | **W** | **N** |
| OCNT-PVIM-ZnPOM (before)* | 87.16 | 8.88 | 0.28 | 0.82 | 2.86 |
| OCNT-PVIM-ZnPOM (after)* | 86.96 | 8.86 | 0.31 | 0.92 | 2.95 |
| *Analysis prior and post to prolonged electrolysis (48 h). | | | | | |

| **Table S6: Crystal data and structure refinement for $Na_8Zn_2$[ZnPOM]** | |
|---|---|
| | **$Na_8Zn_2$[ZnPOM]** |
| empirical formula | $(H_4Na_{14}O_{108}W_{19.02}Zn_{8.98}$ |
| formula weight | 6138.21 |
| temp (K) | 100(2) |
| cryst syst | Triclinic |
| space group | *P* -1 |
| unit cell dimension | |
| *a* (Å) | 12.4391(4) |
| *b* (Å) | 13.6054(4) |
| *c* (Å) | 16.6803(6) |
| *α* (deg) | 82.3040(10) |
| *β* (deg) | 73.5230(10) |
| *γ* (deg) | 64.2110(10) |
| *V* (Å$^3$) | 2437.23(14) |
| *Z* | 1 |
| *ρ* (calcd) (g/cm$^3$) | 4.182 |
| *F* (000) | 2699 |
| cryst size (mm$^3$) | 0.32 x 0.21 x 0.15 |
| index ranges | $-16 \le h \le 16$,<br>$-18 \le k \le 18$,<br>$-22 \le l \le 22$ |
| no. of reflections collected/unique | 74766 / 12166 |
| GOF on $F^2$ | 1.151 |
| final *R* indices ($I > 2\sigma(I)$) | R1 = 0.0300,<br>wR2 = 0.0730 |
| *R* indices (all data) | R1 = 0.0329<br>wR2 = 0.0742 |
| data/restraints/param | 12166 / 0 / 685 |

**References**

(1) Xia, W.; Jin, C.; Kundu, S.; Muhler, M. A highly efficient gas-phase route for the oxygen functionalization of carbon nanotubes based on nitric acid vapor. *Carbon* **2009,** *47*, 919-922.

(2) Kibsgaard, J.; Tsai, C.; Chan, K.; Benck, J. D.; Nørskov, J. K.; Abild-Pedersen, F.; Jaramillo, T. F. Designing an improved transition metal phosphide catalyst for hydrogen evolution using experimental and theoretical trends. *Energy Environ. Sci.* **2015,** *8*, 3022-3029.

(3) Yang, S.; Shao, D.; Wang, X.; Hou, G.; Nagatsu, M.; Tan, X.; Ren, X.; Yu, J. Design of chitosan-grafted carbon nanotubes: evaluation of How the –OH functional group affects Cs+ adsorption. *Mar. Drugs* **2015,** *13*, 3116-3131.

(4) Kibsgaard, J.; Tsai, C.; Chan, K.; Benck, J. D.; Nørskov, J. K.; Abild-Pedersen, F.; Jaramillo, T. F. Designing an improved transition metal phosphide catalyst for hydrogen evolution using experimental and theoretical trends. *Energy Environ. Sci.* **2015,** *8*, 3022-3029.

(5) Beck, J.; Hilbert, T., Ein, altes ‘Rhodiumsulfid mit überraschender Struktur: Synthese, Kristallstruktur und elektronische Eigenschaften von Rh3S4. *Z. Anorg. Allg. Chem.* **2000,** *626*, 72-79.